

Higher-order topological corner states induced solely by onsite potentials with mirror symmetry

Ya-Jie Wu,^{1,*} Wen He,¹ Ning Li,¹ Zhitong Li,^{2,3} and Junpeng Hou^{4,†}

¹*School of Sciences, Xi'an Technological University, Xi'an 710032, China*

²*School of Science, Beijing University of Posts and Telecommunications, Beijing 100876, China*

³*State Key Laboratory of Information Photonics and Optical Communications,*

Beijing University of Posts and Telecommunications, Beijing 100876, China

⁴*Department of Physics, The University of Texas at Dallas, Richardson, Texas 75080, USA*

Higher-order topological insulators have triggered great interests because of exhibitions of non-trivial bulk topology on lower-dimensional boundaries like corners and hinges. While such interesting phases have been investigated in a plethora of systems by tuning staggered tunneling strength or manipulating existing topological phases, here we show that a higher-order topological phase can be driven solely by mirror-symmetric onsite potentials. We first introduce a simple chain model in one dimension that mimics the Su-Schrieffer-Heeger-like model. However, due to the lack of internal symmetries like chiral or particle-hole symmetry, the energies of the topological edge modes are not pinned at zero. Once the model is generalized to two dimensions, we observe the emergence of topological corner modes. These corner modes are intrinsic manifestation of non-trivial bulk band topology protected by mirror symmetry, and thus, they are robust against symmetry-preserved perturbations. Our study provides a concise proposal for realizing a class of higher-order topological insulators, which involves only tuning onsite energies. This can be easily accessible in experiments and provides a different playground for engineering topological corner modes.

I. INTRODUCTION

Since the discovery of quantized multipole insulators, higher-order (HO) topological phases and materials have attracted great interests because of their novel bulk-boundary correspondences [1–6]. In contrast to conventional (or first-order) topological phases, the topologically protected boundary states of HO topological phase exhibit lower dimensions. In other words, r th-order (co-dimension $r \geq 2$) topological phases in d dimensions host $(d - r)$ -dimensional localized states, rather than $d - 1$ dimensional edge states. For example, in two-dimensional (2D) second-order topological insulators, the boundary states manifest as zero-dimensional (0D) corner states. A variety of candidates have been proposed to host HO topological phases [7–33].

Spatial symmetries enrich topological phases from an aspect differing from conventionally internal symmetries (i.e., particle-hole, time-reversal and chiral symmetries) [34]. These topological crystalline phases have been classified in a unified framework [35]. Later, crystalline symmetries have also been shown to play an important role in different types of HO topological insulators and superconductors [24, 36–40]. While there have been different approaches for realizing HO topological phases, most of them are driven from an existing non-trivial first-order topological phase or rely on extending some models similar to Su-Schrieffer-Heeger (SSH) model by adjusting staggered hopping. More recently, a handful of studies have shown that both first-order and HO topological in-

ulators can be driven by tuning non-Hermitian effects including on-site gain and loss rates [41–43]. While non-Hermiticity has brought interesting aspects into topological phases of matter, they are harder to engineer and control in general. Thus, an interesting question naturally arises: whether existing first-order topological phase and non-Hermitian effects are necessary for driving HO topological phases?

In this paper, we answer the above question by enriching the family of HO topological insulators with a class of HO topological phases induced solely by real and mirror-symmetric onsite potentials. We first introduce a one-dimensional (1D) chain with mirror symmetry and show that a topological phase can be driven through only onsite energy difference between sublattices. Contrary to the usual SSH model and its derivatives, our model is protected by mirror symmetry, instead of chiral symmetry, and thus, the edge modes have non-zero energies. We then generalize the 1D model to a Wannier-type second-order topological insulator, which is driven from a Dirac semimetal by only onsite potentials. Such a topologically non-trivial phase can be characterized by Wannier centers. To show the flexibility of the proposed platform, we further present an intrinsic second-order topological insulator on a square lattice and characterize its topology using edge polarizations and quadrupole moment. Finally, to confirm the topological protection of this class of second-order topological insulators, we impose mirror-symmetry-preserved perturbations and show that the corner modes are robust up to a global energy shift.

This paper is organized as follows. In Sec. II, we introduce a 1D lattice with inversion symmetric onsite potentials, which serves as the base for our HO topological models. In Sec. III, we start with a honeycomb

*wuyajie@xatu.edu.cn

†ryanhou@fb.com

lattice with mirror-symmetric onsite potentials, and explore the HO topological phases. In Sec. IV, we turn to the study of a square lattice, and introduce edge polarizations and quadrupole moment to characterize the corresponding HO topological phase. Conclusions and discussions are drawn in Sec. V.

II. 1D SUPERLATTICE WITH MIRROR-SYMMETRIC POTENTIALS

For simplicity, we consider a 1D superlattice consisting of two sublattice sites with different onsite potentials V_a and V_b , while inter- and intra-site coupling t is uniform. A minimal non-trivial model with mirror (inversion) symmetry has a unit cell (V_a, V_b, V_a) . Here for better demonstration, we use a configuration of (V_a, V_b, V_b, V_a) , as shown in Fig. 1 (a), and the corresponding system Hamiltonian in momentum space reads

$$h(k) = \frac{t}{2}(1 + \cos k)\sigma_x\tau_x + \frac{t}{2}(1 - \cos k)\sigma_y\tau_y + t\sigma_0\tau_x + \frac{t}{2}\sin k(\sigma_y\tau_x + \sigma_x\tau_y) + V_-\sigma_z\tau_z + V_+\sigma_0\tau_0(1)$$

under the basis $\hat{\psi}_k = (\hat{a}_{1,k}, \hat{a}_{2,k}, \hat{a}_{3,k}, \hat{a}_{4,k})^T$, where $V_{\mp} = (V_a \mp V_b)/2$, σ_0 and τ_0 are identity matrices. The Hamiltonian $h(k)$ preserves mirror symmetry with $\mathcal{M}h(k)\mathcal{M}^{-1} = h(-k)$, where $\mathcal{M} = \sigma_x\tau_x$. In the following, we set $V_+ = 0$, i.e., $V_a = -V_b = V > 0$ without loss of generality since V_+I only shifts the energy bands globally, but doesn't change the topological number of each bands because the eigenvectors remain invariant. The four energy bands are given by

$$E_{\pm,+} = \pm\sqrt{2t^2 + V^2 + \sqrt{2t^2(t^2 + 2V^2 + t^2\cos k)}},$$

$$E_{\pm,-} = \pm\sqrt{2t^2 + V^2 - \sqrt{2t^2(t^2 + 2V^2 + t^2\cos k)}}.$$

When $V = 0$, there are four gapless energy bands as shown in Fig. 1 (b). The bands $E_{+,+}$ ($E_{-,+}$) and $E_{+,-}$ ($E_{-,-}$) touch at momentum point $k = \pi$, and the bands $E_{+,-}$ and $E_{-,-}$ touch at $k = 0$ with linear dispersions. As V increases, the bands $E_{+,+}$ ($E_{-,+}$) and $E_{+,-}$ ($E_{-,-}$) are separated with an energy gap $\Delta E_{g1} = \sqrt{t^2 + (t+V)^2} - \sqrt{t^2 + (t-V)^2}$ at $k = \pi$, and there opens an energy gap $\Delta E_{g2} = \sqrt{t^2 + V^2} - t$ between $E_{+,-}$ and $E_{-,-}$ at $k = 0$ (see Fig. 1 (c)).

Since the 1D superlattice preserves mirror symmetry, each energy band would contribute a quantized topological invariant. We define the topological invariant as

$$\eta = -\frac{1}{\pi} \oint \mathcal{A}_k dk_x, \quad (2)$$

with $\mathcal{A}_k = -i \langle u_{m,k} | \partial_{k_x} u_{n,k} \rangle$. After calculations, we find that $\eta = 0, 0, 1, -1$ for bands $E_{-,+}$, $E_{-,-}$, $E_{+,-}$ and $E_{+,+}$, respectively. The topological invariants can also be

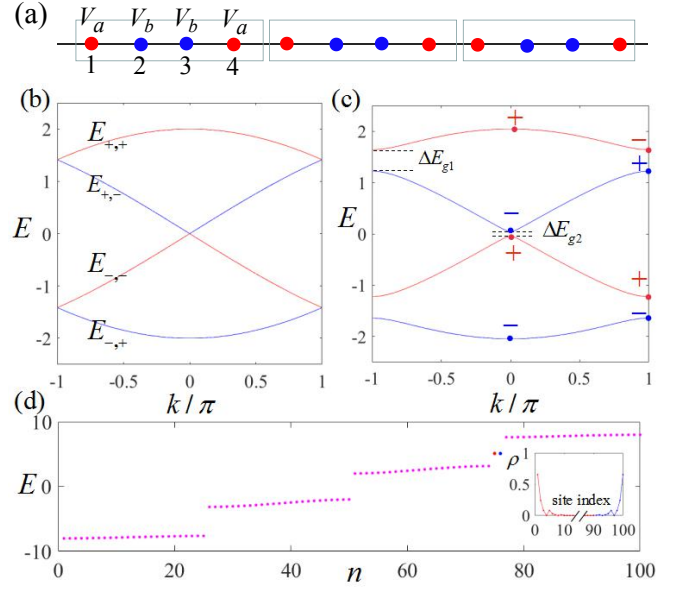


FIG. 1: (a) Illustration of 1D lattice with onsite potentials V_a and V_b . (b) and (c) Energy spectra at different onsite potentials with $V = 0$ and $V = 0.3$. (d) Eigenenergies for 1D chain with 100 sites and $V = 4.0$ under open-boundary conditions. n denotes eigenstate index. The inset showcases the particle density versus site index for states indicated by blue and red dots in (d).

equivalently defined by $\eta = -[m(0) - m(\pi)]/2$, where $m(0)$ and $m(\pi)$ are parities at momentum points $k = 0$ and π , respectively. In Fig. 1 (d), we denote even and odd parity as "+" and "-", respectively. We can also obtain consistent topological invariants for each band with that from Eq. (2).

To present the bulk-boundary correspondence, we calculate energies for a lattice under open boundary conditions. The energy level distributions are shown in Fig. 1 (d). It shows that two states emerge in the gap between the third band and fourth band from bottom to top. The inset of Fig. 1 (d) presents the particle density for these two states, which shows that these two in-gap states are localized at two ends of lattices, similar to the celebrated SSH model. This behavior confirms the bulk-boundary correspondence for this topological system.

When $V < 0$, the topological invariants for bands $E_{-,+}$, $E_{-,-}$, $E_{+,-}$ and $E_{+,+}$ would be changed to 1, -1, 0, 0, and two localized states emerge in the gap between the first and second band from bottom to top. In this sense $V = 0$ is a critical topological phase transition point for each energy band.

III. 2D HONEYCOMB LATTICE WITH MIRROR-SYMMETRIC POTENTIALS

We consider a graphene lattice with mirror-symmetric onsite potentials (V_a, V_b, V_b, V_a) along x , as shown in

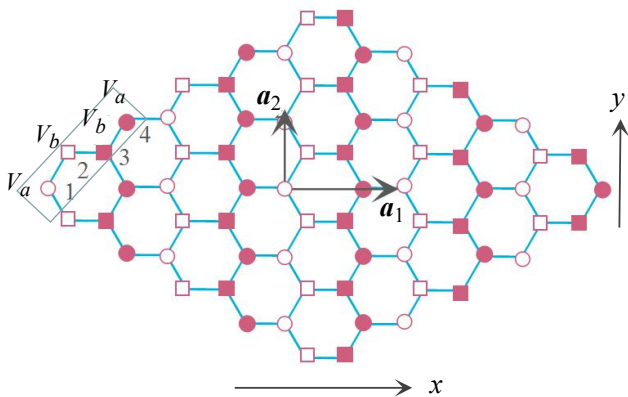


FIG. 2: Illustration of a honeycomb lattice with mirror-symmetric potentials along x . Each unit-cell consists of four sublattice sites indexed by 1 – 4.

Fig. 2. The single-particle Hamiltonian is written as $\hat{H} = \hat{H}_0 + \hat{H}_p$. The first term on r.h.s. reads $\hat{H}_0 = -t \sum_{\langle i_m, j_n \rangle} (\hat{a}_{i_m}^\dagger \hat{a}_{j_n} + h.c.)$ with t the coupling between nearest-neighbor sites $\langle i_m, j_n \rangle$, and the mirror-symmetric potential is described by $\hat{H}_p = \sum_{m,i} V_m \hat{a}_{i_m}^\dagger \hat{a}_{i_m}$ with $V_{m=1,4} = V_a$ and $V_{m=2,3} = V_b$ representing the mirror symmetric onsite potentials. The operator $\hat{a}_{i_m}^\dagger$ (\hat{a}_{i_m}) creates (annihilates) a mode at site i_m . The mirror-symmetric onsite potentials enlarge the unit-cell of the usual honeycomb lattice. Each unit-cell consists of four sublattices. The Bravais vectors are now described by $\mathbf{a}_1 = (3, 0)$ and $\mathbf{a}_2 = (0, \sqrt{3})$, as shown in Fig. 2. The first Brillouin zone (BZ) decreases correspondingly. Here we have set the lattice spacing of the honeycomb lattice to be unit. The total Hamiltonian H in momentum space can be written as $\hat{H} = \sum_k \hat{\psi}_k^\dagger h(k) \hat{\psi}_k$ under the basis $\hat{\psi}_k = (\hat{a}_{1,k}, \hat{a}_{2,k}, \hat{a}_{3,k}, \hat{a}_{4,k})^T$ with

$$h(k) = \alpha_k \sigma_0 \tau_x - t \sin k_{a_2} \sigma_0 \tau_y + \beta_k \sigma_x \tau_x + \gamma_k \sigma_y \tau_y + \frac{t}{2} \sin k_{a_3} (\sigma_x \tau_y + \sigma_y \tau_x) + V_- \sigma_z \tau_z + V_+ I \quad (3)$$

where $\alpha_k = t [1 + \cos(\sqrt{3}k_y)]$, $\beta_k = \frac{1}{2}t(1 + \cos k_{a_3})$, $\gamma_k = \frac{1}{2}t(1 - \cos k_{a_3})$, $k_{a_2} = \sqrt{3}k_y$, $k_{a_3} = \mathbf{k} \cdot (\mathbf{a}_1 + \mathbf{a}_2) = 3k_x + \sqrt{3}k_y$, and $I = \sigma_0 \tau_0$.

When $V_a = V_b$, the Hamiltonian \hat{H} preserves inversion symmetry $\mathcal{P} = \sigma_x \tau_x \mathcal{U}$, time-reversal symmetry $\mathcal{T} = \mathcal{K} \mathcal{U}$ and C_3 rotation symmetry, where $\mathcal{U} = \text{diag}(e^{ikb_1 - ik\frac{b_3}{2}}, e^{-ik\frac{b_3}{2}}, e^{ik\frac{b_3}{2}}, e^{-ikb_1 + ik\frac{b_3}{2}})$ is a diagonal unitary matrix and \mathcal{K} is a conjugation operator. These symmetries lead to the system hosting two locally and globally stable Dirac points with geometric phases $\pm\pi$.

When $V_a \neq V_b$, C_3 symmetry would be broken and Dirac points may be gapped. However, in this case the model also preserves mirror symmetries, i.e., $\mathcal{M}_{x/y} h(k_{x/y}) \mathcal{M}_{x/y}^{-1} = h(-k_{x/y})$ with $\mathcal{M}_x = \sigma_x \tau_x \mathcal{U}$ and $\mathcal{M}_y = \sigma_0 \tau_0 \mathcal{U}$. Without loss of generality, we again set

$V_a = -V_b = V$ in the following. The four energy bands in momentum space are solved as

$$E_{\pm,+}(k) = \pm \sqrt{V^2 + t^2 (3 + 2 \cos \sqrt{3}k_y)} + 2\sqrt{\alpha_k},$$

$$E_{\pm,-}(k) = \pm \sqrt{V^2 + t^2 (3 + 2 \cos \sqrt{3}k_y)} - 2\sqrt{\alpha_k},$$

where $\alpha_k = t^2 (t^2 + V^2 + t^2 \beta_k)$ with $\beta_k = \cos 3k_x + (1 + \cos 3k_x) \cos \sqrt{3}k_y$.

Compared to the conventional graphene model with $V = 0$, the energy bands are folded and Dirac points shift to $\mathbf{K} = (0, 2\sqrt{3}\pi/9)$ and $\mathbf{K}' = (0, -2\sqrt{3}\pi/9)$ as plotted in Fig. 3(a₁). As the potential V increases, two Dirac points remain massless while they approach each other in momentum space because the local stability is protected by \mathcal{P} and \mathcal{T} symmetries. They merge at the time-reversal-invariant point $(0, \pi/\sqrt{3})$ at $V = V_{c1} = t$, as shown in Fig. 3(b₁). If V increases further, an energy gap opens as shown in Fig. 3(c₁). In the following, we will showcase the topological nature for each energy band.

A. Topological bands and topological invariants

From above symmetry analysis, both $\mathcal{P}\mathcal{T}$ symmetry and mirror symmetry are respected along x for the system. The mirror symmetry \mathcal{M}_x guarantees the non-trivial quantization of polarization along the x direction. To present the polarization as the bulk property, we construct a Wilson loop operator $\mathcal{W}_{x,k}$ in the x direction, where k represents the base point of the loop. We define the Bloch wave function of the occupied energy bands with negative energies as $|u_{m,k}\rangle$, where $H(k)|u_{m,k}\rangle = E_m(k)|u_{m,k}\rangle$ with normalization condition $\langle u_{m,k} | u_{n,k'} \rangle = \delta_{m,n} \delta_{k,k'}$. The Wilson loop operator is described by $W_{x,k} = F_{x,k+N_x \Delta k_x} \dots F_{x,k+\Delta k_x} F_{x,k}$, where the elements for $F_{x,k}$ are defined by $[F_{x,k}]^{m,n} = \langle u_{m,k+\Delta k_x} | u_{n,k} \rangle$ with $\Delta k_x = 2\pi/N_x$ and N_x the number of unit cells in the x direction. The topological invariant at each k_y is then defined by $\eta_x(k_y) = -\frac{i}{\pi} \text{Tr}(\ln W_{x,k})$, which forms the Wannier band. It is quantized under mirror symmetries. In the thermodynamic limit, the topological invariant $\eta_x(k_y)$ is given by

$$\eta_x(k_y) = -\frac{1}{\pi} \text{Tr} \left(\oint \mathcal{A}_k dk_x \right), \quad (4)$$

where \mathcal{A}_k is a non-Abelian Berry connection with $(\mathcal{A}_k)_{mn} = -i \langle u_{m,k} | \partial_{k_x} u_{n,k} \rangle$. Following similar steps, the topological invariant $\eta_y(k_x)$ could be obtained at each k_x . Finally, the topological invariant, namely the Wannier center of Wannier bands is defined as (η'_x, η'_y) with $\eta'_{x/y} = \frac{1}{4b_{y/x}} \oint \eta(k_{y/x}) dk_{y/x}$, where the reciprocal vectors are $b_x = \pi/3$ and $b_y = \pi/\sqrt{3}$.

When $V = 0$, \hat{H} becomes a conventional graphene model. The topological invariant for the band $E_{-,-}$ is $\eta_{x,-,-}(k_y) = 1$ if $-\pi/\sqrt{3} < k_y < -2\sqrt{3}\pi/9$ or $2\sqrt{3}\pi/9 < k_y < \pi/\sqrt{3}$ and $\eta_{x,E_{-,-}}(k_y) = 0$ otherwise. The topological invariant for the band $E_{+,-}$ is $\eta_{x,E_{+,-}}(k_y) = 0$ if $-\pi/\sqrt{3} < k_y < -2\sqrt{3}\pi/9$ or $2\sqrt{3}\pi/9 < k_y < \pi/\sqrt{3}$ and $\eta_{x,E_{+,-}}(k_y) = 1$ otherwise. The topological invariants for the bands $E_{+,+}$ and $E_{-,-}$ are $\eta_{x,E_{-,-}}(k_y) = 0$ for any k_y , as plotted in Fig. 3(a₂). For $V = V_{c1} = t$, the energy gap closes at momentum lines $k = (k_x, \pi/\sqrt{3})$ with any k_x , as presented in Fig. 3(b₁). The topological invariants for each band has been shown in Fig. 3(b₁), where $\eta_{x,E_{+,-}}(\pm\pi/\sqrt{3})$ and $\eta_{x,E_{-,-}}(\pm\pi/\sqrt{3})$ are not well defined indicated by the dashed lines. When $V > V_{c1}$, the energy gap opens between bands $E_{+,-}$ and $E_{-,-}$. We find $\eta_{x,E_{+,+}}(k_y) = -1$, $\eta_{x,E_{+,-}}(k_y) = 1$, $\eta_{x,E_{-,-}}(k_y) = 0$, and $\eta_{x,E_{-,+}}(k_y) = 0$ for any k_y [see Fig. 3(c₂)]. Namely, when $V > V_{c1}$, the Wannier centers of the bands $E_{+,-}$, $E_{-,-}$ and $E_{-,+}$ are $\eta'_{y,E_{+,-}} = 1/2$, $\eta'_{y,E_{-,-}} = 0$, $\eta'_{y,E_{-,+}} = 0$, respectively.

Therefore, if $V > V_{c1}$, the total Wannier center of the lowest three Wannier bands is quantized to a non-trivial value $(1/2, 0)$ with lowest three energy bands ($E_{+,-}$, $E_{-,-}$ and $E_{-,+}$) being occupied. We dubbed this phase as second-order topological phase A (SOTA). Similar cases happen when $V < V_{c2} = -t$, where we observe that the bands $E_{+,+}$ and $E_{+,-}$ become topologically trivial, while bands $E_{-,-}$ and $E_{-,+}$ are topologically non-trivial. These lead to that the Wannier center becomes $(1/2, 0)$ if the bands $E_{-,-}$ is occupied. This phase is referred to second-order topological phase B (SOTB). In summary, the topological phase diagram is shown in Fig. 3(d).

Here, we would like to point out that the quantization of topological invariant η'_x is guaranteed by mirror symmetry along the x direction. It is robust against weak mirror-symmetric perturbations as long as the corresponding energy gap doesn't close.

B. Topological corner modes and interface modes

Consider a sample shown in Fig. 4(a). We set the parameter $V > V_{c1}$ so that the system is in a topological phase SOTA with the Wannier center quantized to $(1/2, 0)$. First take the case $V = 2.0$ as an example and its numeric results are plotted in Fig. 4(a) and (c). Two degenerate modes indicated by the blue dots emerge in the energy gap as shown in Fig. 4(c). The corresponding particle density distributions have been shown in Fig. 4(a). It presents that the two degenerate modes are localized at two horizontal corners of the given sample. Fig. 4(b) shows the case $V = 5.5$, in which the corner modes become more localized as the strength of potential increases. Similarly, we observe that the topological corner modes also exist when $V < V_{c2}$ in topological phase SOTB.

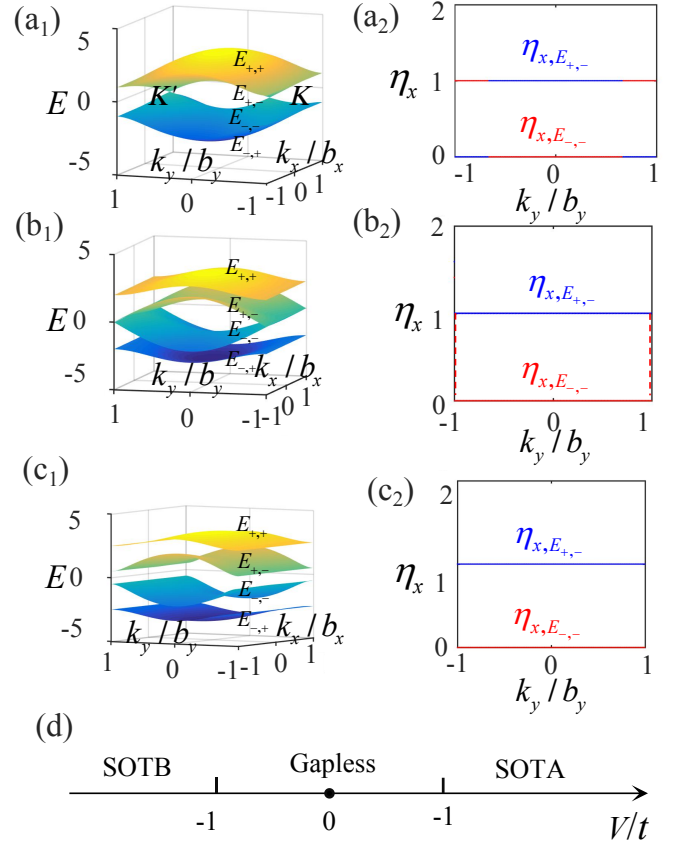


FIG. 3: (a₁)-(c₁) Energy spectra at different onsite potentials. (a₂)-(c₂) Topological invariants for the energy band $E_{-,-}$ (red lines) and the energy band $E_{+,-}$ (blue lines) corresponding to (a₁)-(c₁). The strength for each case is (a₁) and (a₂) $V = 0$, (b₁) and (b₂) $V = 1.0$, (c₁) and (c₂) $V = 1.5$. (d) Phase diagram versus V/t . Other parameters are set to be $t = 1$, $b_x = \pi/3$, and $b_y = \pi/\sqrt{3}$.

So far, we have focused on the special case with $V_a = -V_b$. We remarked that the quantization of a non-trivial topological invariant (Wannier center) is guaranteed by the mirror symmetry. It means that it is also respected when $V_a \neq V_b$ since $V_+ = (V_a + V_b)/2$ only shifts energies globally and $V_- = (V_a - V_b)/2$ determines the wave functions. Therefore, it is expected that the system is non-trivial when $|V_-| > V_{c1}$, as long as the energy gap between nearby bands remains open. Here, we also would like to remark that while the mirror-symmetric potential perturbations may shift energies of corner modes, the Wannier center of the system is invariant, and the corner modes remain localized. This is different from conventional HO topological system where the energies of corner modes are usually pinned at zero.

As discussed above, a graphene model with appropriate mirror-symmetric potentials V is a HO topological insulator characterized by Wannier center $(1/2, 0)$. In the following, we consider two graphene sheets separated by a domain wall as sketched in Fig. 5(a). Here the translation symmetry of graphene lattice is broken along

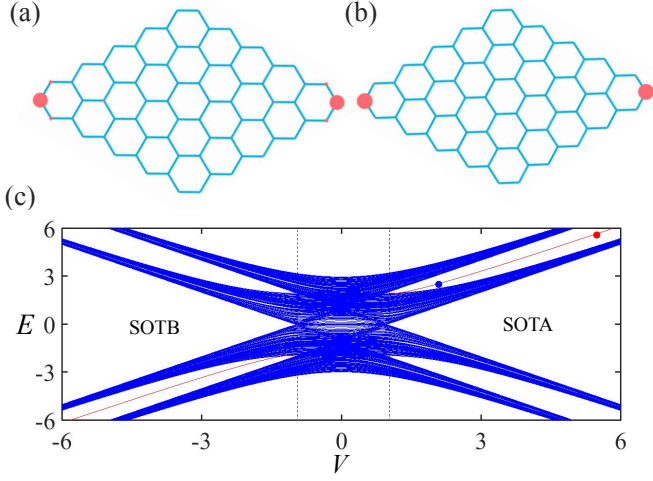


FIG. 4: (a) Spatial density distribution of the corner modes with $V = 2$ indicated by blue dot in (c) and the radii of the pink disk is proportional to local density. (b) Similar to (a) but plotted with a different onsite potential $V = 5.5$ indicated by red dot in (c), demonstrating the corner modes become more localized as the strength of onsite potential increases. (c) Eigenspectrum versus onsite potential V . The red lines denote two-fold degenerate corner modes. Common parameter is set to be $t = 1$.

x direction, but the translation symmetry is respected along y . In the following, we take k_y as a system parameter and treat $\hat{H}(k_y)$ as a quasi-one dimensional chain. The Hamiltonian \hat{H} is then written as

$$\hat{H} = \sum_{k_y} \hat{H}(k_y) = \sum_{k_y} \hat{H}_0(k_y) + \hat{H}_p(k_y), \quad (5)$$

with

$$\begin{aligned} \hat{H}_0(k_y) &= -t \sum_{i_x} \hat{a}_{1,i_x,k_y}^\dagger \hat{a}_{4,i_x-1,k_y} + \epsilon_{k_y} \hat{a}_{1,i_x,k_y}^\dagger \hat{a}_{2,i_x,k_y} \\ &\quad + \hat{a}_{2,i_x,k_y}^\dagger \hat{a}_{3,i_x,k_y} + \epsilon_{k_y}^* \hat{a}_{3,i_x,k_y}^\dagger \hat{a}_{4,i_x,k_y} + h.c., \\ H_p(k_y) &= \sum_{m,i_x} V_m \gamma_m a_{m,i_x,k_y}^\dagger a_{m,i_x,k_y} \end{aligned} \quad (6)$$

where $\epsilon_{k_y} = t(1 + e^{i\sqrt{3}k_y})$ and the domain wall structure is given by $\gamma_{m=1,4} = -\gamma_{m=2,3} = 1$ (left-hand side of the domain wall) and $\gamma_{m=1,4} = -\gamma_{m=2,3} = -1$ (right-hand side), as depicted in Fig. 5(a).

The energy spectra of the system can be derived from $\hat{H}(k_y)|u(k_y)\rangle = E(k_y)|u(k_y)\rangle$. We set the strength of appropriate potentials so that both graphene sheets are in different topological phases, i.e., the left and right ones are in SOTA and SOTB, respectively. Through numerical calculations, we obtain energy spectra of graphene sheets as shown in Fig. 5(b), and observe localized states at the interface, i.e., the states with positive and negative energies localizing at the left-hand and right-hand side of the domain wall, respectively, as plotted in Fig. 5(c) and (d). This confirms that two different topological

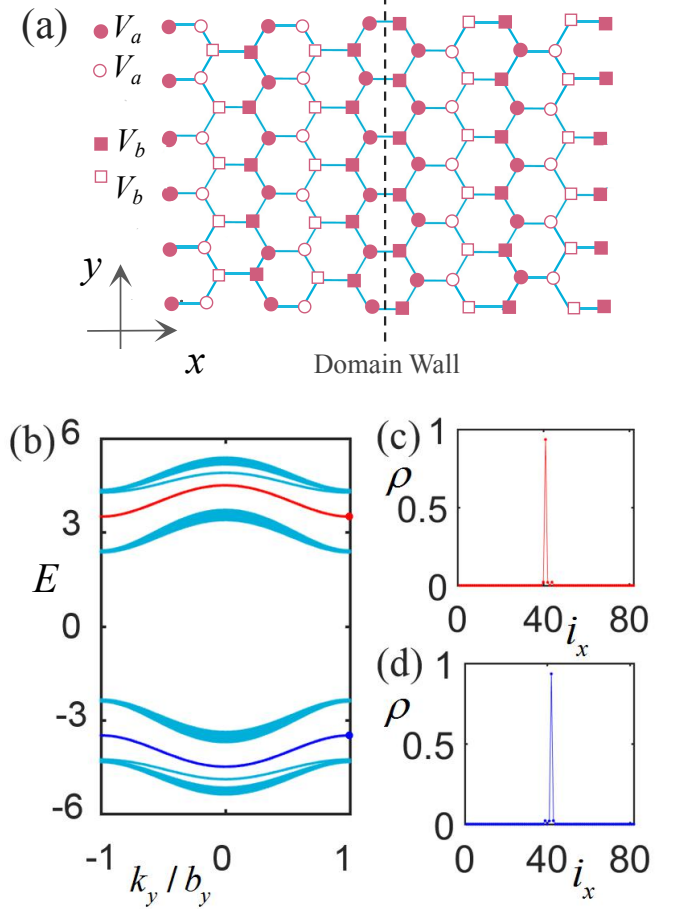


FIG. 5: (a) Two graphene sheets with a domain wall in between, which is highlighted by the dashed line. As they possess opposite topological invariants, topological interface modes near the domain wall naturally arise. (b) Energy spectra versus k_y for two graphene sheets with a domain wall in between and an open-boundary condition along x (total $N_x = 82$ sites). The blue and red curves indicate the interface modes. (c) and (d) depict the density distribution of two localized interface states. We set parameters $t = 1$ and $V = 3.2$.

phases (SOTA and SOTB) indeed exhibit different topological properties and such a setup can be used as the experimental setup of photonic higher-order topological insulators in graphene lattices.

For a domain-wall structure, we may also consider the general case (V_a, V_b, V_b, V_a) with $V_a \neq -V_b$. The numeric calculations also demonstrate the existence of topological localized interface modes. Finally, we also consider mirror-symmetric perturbations and find that, although the energies of localized states and bulk states vary, the topological interface states always localize at the domain wall. In this sense, the topological interface states are robust and mirror-symmetry protected.

IV. 2D SQUARE LATTICE WITH MIRROR-SYMMETRIC POTENTIALS

We now consider a square lattice with mirror-symmetric potentials and each square plaquette enclosing a π flux, as shown in Fig. 6 (a). The Hamiltonian is written as

$$h(k) = t\sigma_+^x\sigma_-^x\sigma_0^y\sigma_0^y + t\sigma_0^x\sigma_+^x\sigma_0^y\sigma_0^y + te^{-ik_x}\sigma_+^x\sigma_+^x\sigma_0^y\sigma_0^y \\ + t\sigma_0^x\sigma_-^x\sigma_+^y\sigma_-^y + t\sigma_0^x\sigma_x^x\sigma_0^y\sigma_+^y + te^{-ik_y}\sigma_0^x\sigma_x^x\sigma_z^y\sigma_+^y \\ + h.c. + V\sigma_z^x\sigma_z^x\sigma_z^y\sigma_z^y, \quad (7)$$

where t and V denote the coupling between nearest-neighbor sites and onsite potential, respectively. σ^x and σ^y are Pauli matrices acting on the degrees of freedom spanned along x and y , respectively, while σ_0^x and σ_0^y are identity matrices. The ladder operator σ_\pm^x reads $\sigma_\pm^x = (\sigma^x \pm i\sigma^y)/2$ and σ_\pm^y is defined similarly. The Hamiltonian preserves mirror symmetries along both x and y as $\mathcal{M}'_x H(k_x, k_y) \mathcal{M}'_x{}^{-1} = h(-k_x, k_y)$ and $\mathcal{M}'_y h(k_x, k_y) \mathcal{M}'_y{}^{-1} = h(k_x, -k_y)$, where $\mathcal{M}'_x = \sigma_x^x\sigma_x^x\sigma_0^y\sigma_z^y$ and $\mathcal{M}'_y = \sigma_0^x\sigma_0^x\sigma_x^y\sigma_x^y$. There are eight pairs of energy bands and each pair is doubly degenerate. When $V = 0$, the two central energy bands touch at Dirac point $\Gamma = (0, 0)$. When $V \neq 0$, an energy gap opens at Γ with the gap $\Delta E_g = 2(\sqrt{V^2 + 2t^2} - \sqrt{2}t)$. In addition, there also opens a gap between the first-two pairs and second-two pairs of bands from top to bottom as potential V increases, which implies that the topological phase transition may occur with opening the gap.

Consider a square sample with 36×36 sites with $V = 3.0$. We compute its eigenenergy level distributions as shown in Fig. 6(c). It showcases that there are four energy modes in the energy gap. After plotting the particle density distributions (see Fig. 6(b)), we find these modes are localized at four corners of the sample.

To characterize the topological properties of corner states, we compute the edge polarizations $p_x^{\text{edge},y}$ ($p_y^{\text{edge},x}$) using Wilson loops on a torus geometry where the lattice has open boundary along y (x) but periodic boundary along x (y). The polarization distribution along y is defined by [1, 4]

$$p_x(i_y) = \frac{1}{N_x} \sum_{j,k_x,\alpha,n} \left| [u_{k_x}^n]^{i_y,\alpha} [v_{k_x}^j]^{i_y,\alpha} \right|^2 \nu_x^j. \quad (8)$$

Here N_x is the number of unit-cell along the x direction. $[u_{k_x}^n]^{i_y,\alpha}$ denotes the (i_y, α) -th component of occupied state $|u_{k_x}^n\rangle$, where i_y and α are the site index along y and sublattice degrees of freedom along x , respectively. $[v_{k_x}^j]^n$ is the n th component of j th eigenvector corresponding to the Wannier values ν_x^j of the Wannier Hamiltonian $H_{\mathcal{W}_x} = -i \ln \mathcal{W}_x$. \mathcal{W}_x represents the Wilson loop operator, i.e., $\mathcal{W}_x = F_{x,k_x+(N_x-1)\Delta k_x} \dots F_{x,k_x+\Delta k_x} F_{x,k_x}$ with $[F_{x,k_x}]^{mn} = \langle u_{k_x+\Delta k_x}^m | u_{k_x}^n \rangle$ and $\Delta k_x = 2\pi/N_x$.

Figure 6(d) presents the edge polarization $p_x(i_y)$ versus site index i_y with $V = 3$ and the occupied state

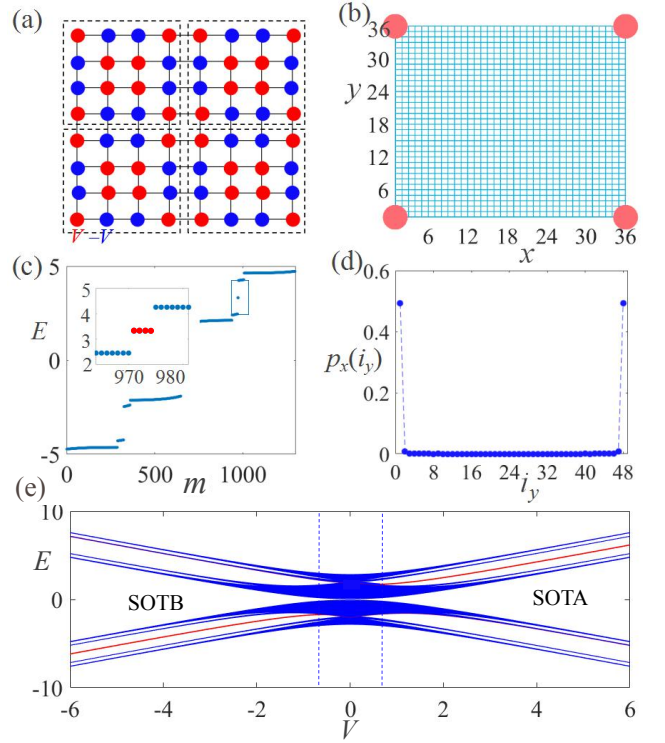


FIG. 6: (a) Illustration of a square lattice with mirror-symmetric potentials. Each unit-cell consists of sixteen sublattice sites. (b) Spatial density distribution of the corner modes indicated in (c). The radii of spots is proportional to the particle density. (c) Eigenenergy level distributions for a 36×36 lattice. The inset shows enlarge portion of rectangle in (c), where four red dots indicate corner modes. (d) Edge polarizations for a configurations with open boundary along x but periodic boundary along y . Common parameters are $t = 1$, $V = 3$ in (b)-(d). (e) Eigenenergies versus potential V . The red lines in SOTA and SOTB represent four-fold degenerate corner modes.

number $n_{occ} = 4n_y * 3/4$, where n_y is the site number along y . Similar results are obtained on a torus geometry where the lattice has open boundary along x but periodic boundary along y . These results implies that localized modes exist at the corners of the sample, consistent with the results in Fig. 6(b) and (d).

In addition, this topological phase can also be characterized by quadrupole moment [30]. We consider N_o states are occupied represented as $|\chi_l\rangle = \sum_{j\alpha} \phi_{l,j\alpha} |j\alpha\rangle$, where $l = 1, \dots, N_o$, and $j\alpha$ denotes indices of unit-cells and sublattice sites with $j = 1, \dots, N_u$ and $\alpha = 1, 2, \dots, 16$. By arranging N_o occupied state columnwise, we construct a unitary matrix U with dimension $16N_u \times N_o$. The density of particles is defined by

$$n = -\frac{i}{2\pi} \text{Tr} \ln U^\dagger O U. \quad (9)$$

Here O is a diagonal $16N_u \times 16N_u$ dimensional matrix with elements $O_{4(j-1)+\alpha_x, 4(j-1)+\alpha_y} = \exp(i2\pi x_{j\alpha_x} y_{j\alpha_y} / N_x N_y)$, where N_x and N_y are

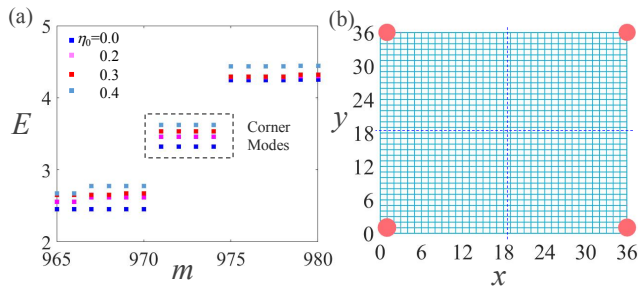


FIG. 7: (a) Eigenenergies E versus the state index m in the presence of mirror-symmetric random potentials with different amplitude η_0 . (b) The particle density distributions of in-gap modes indicated by the red square in dashed box in (a) with $\eta_0 = 0.3$. Blue dashed lines represent two mirrors along x and y . Common parameter is set to be $t = 1$.

unit-cell numbers along x and y , and $\alpha_x, \alpha_y = 1, 2, 3, 4$. To characterize the topological properties, we subtract the contribution of density in the atomic limit, represented by $n_{at} = n_f \sum_{j\alpha_x\alpha_y} x_{j\alpha_x} y_{j\alpha_y} / (N_x N_y)$ with $n_f = N_o / (16N_u)$, and define quadrupole moment as $Q_{xy} = n - n_{at} \pmod{1}$. Through numeric calculations with periodic boundary conditions, we obtain $Q_{xy} = 1/2$ with $N_o = 16N_u * 3/4$ when $V = 3$, indicating a second-order topological phase emerges driven by mirror-symmetric potentials. We dubbed this phase as SOTA phase, as shown in Fig. 6 (e).

Finally, we plot eigenenergies versus potential V , and observe topological corner modes indicated by red lines with four-fold degenerates in both SOTA and SOTB phases, as shown in Fig. 6 (e). We would like to remark that this HO phase is robust against weak mirror-symmetric perturbations while the energies of corner modes may globally shift (see Appendix for details).

V. CONCLUSION AND DISCUSSION

In contrast to most of previous proposals to implement higher-order topological phases, we introduce an interesting and accessible platform for engineering and controlling HO topological phases by solely tuning real onsite potentials. The topological corner modes are in the band energy gap and localize at 0D boundaries. In the presence of mirror-symmetric disorders, this HO topological phase is robust in the sense that the in-gap localized modes remain at corners and topological invariant doesn't change, while the energies of in-gap corner modes shift since this model doesn't preserve chiral symmetry or particle-hole symmetry. Our proposed model can be readily implemented in a range of systems like cold atoms, optics and acoustics. The proposed models also provides a playground for studying novel topological phenomena with, for example, non-Hermitian effects or nonlinear interac-

tions.

In summary, we have studied HO topological phases induced solely by mirror-symmetric onsite potentials. The model can also be generalized to implementing third-order topological phases in three dimensions. Because manipulating onsite energies are accessible in most experimental platforms and our proposal does not require fine tuning of hopping strength, our scheme provides a realistic playground for the experimental study of HO topological phases in both quantum and classical systems.

Acknowledgments

This work is supported by the Scientific Research Program Funded by the Natural Science Basic Research Plan in the Shaanxi Province of China (Programs No. 2021JM-421 and No. 2019JM-001), the NSFC under the Grant No. 11504285, the Scientific Research Program Funded by Shaanxi Provincial Education Department under the grant No. 18JK0397, and the Young Talent fund of the University Association for Science and Technology in Shaanxi, China (Program No. 20170608).

Appendix A: Robustness of corner states against perturbations

We consider two cases to show the robustness of corner states against perturbations. First we impose mirror-symmetric perturbation on onsite potentials described as $\hat{H}_{ap} = \sum_i \eta_i \hat{a}_i^\dagger \hat{a}_i$, where $\eta_{i=(x,y)} = \eta_0 \kappa_{i_x, i_y}$, η_0 is the amplitude of the random potential, and $\kappa_{i_x, i_y} = \kappa_{N_x - i_x + 1, N_y - i_y + 1} \in [0, 1]$ is a random quantity for $i_x \leq N_x/2$ and $i_y \leq N_y/2$ (see Fig. 7(b)). We take a 36×36 square lattice as an example and numerically compute its energies, as shown in Fig. 7(a). We observe that the energies for four in-gap states acquire a finite energy shift. We showcase the density distribution of these four states in Fig. 7(b). It shows that they remain localized at four corners of the sample, which indicates the induced second-order topological phase with corner modes are robust.

We next consider the general random perturbation on onsite potentials represented as $H_{bp} = \sum_i \delta_i a_i^\dagger a_i$, where $\delta_i = \delta_0 \kappa_i$, $\kappa_i \in [0, 1]$ is a random number. Through numeric calculations we find four in-gap states may acquire different energies. It implies the corner states no longer have the same energies in the absence of mirror symmetries. However, these modes remain localized at corners as long as they are in the band-gap.

To summarize, the corner states are robust against mirror-symmetric perturbations, but they acquire same non-zero energies.

- [1] W. A. Benalcazar, B. A. Bernevig, and T. L. Hughes, Quantized electric multipole insulators, *Science* **357**, 61(2017).
- [2] Z. Song, Z. Fang, and C. Fang, $(d - 2)$ -Dimensional Edge States of Rotation Symmetry Protected Topological States, *Phys. Rev. Lett.* **119**, 246402 (2017).
- [3] J. Langbehn, Y. Peng, L. Trifunovic, F. von Oppen, and P. W. Brouwer, Reflection-Symmetric Second-Order Topological Insulators and Superconductors, *Phys. Rev. Lett.* **119**, 246401 (2017).
- [4] W. A. Benalcazar, B. A. Bernevig, and Taylor L. Hughes, Electric multipole moments, topological multipole moment pumping, and chiral hinge states in crystalline insulators, *Phys. Rev. B* **96**, 245115 (2018).
- [5] S. Franca, J. van den Brink, and I. C. Fulga, An anomalous higher-order topological insulator, *Phys. Rev. B* **98**, 201114(R) (2018).
- [6] H. Li and K. Sun, Pfaffian Formalism for Higher-Order Topological Insulators, *Phys. Rev. Lett.* **124**, 036401 (2020).
- [7] M. Ezawa, Higher-Order Topological Insulators and Semimetals on the Breathing Kagome and Pyrochlore Lattices, *Phys. Rev. Lett.* **120**, 026801 (2018).
- [8] M. Ezawa, Topological Switch between Second-Order Topological Insulators and Topological Crystalline Insulators, *Phys. Rev. Lett.* **121**, 116801 (2018).
- [9] M. Ezawa, Minimal models for Wannier-type higher-order topological insulators and phosphorene, *Phys. Rev. B* **98**, 045125 (2018).
- [10] F. Liu, H.-Y. Deng, and K. Wakabayashi, Helical Topological Edge States in a Quadrupole Phase, *Phys. Rev. Lett.* **122**, 086804 (2019).
- [11] H. Fan, B. Xia, L. Tong, S. Zheng, and D. Yu, Elastic Higher-Order Topological Insulator with Topologically Protected Corner States, *Phys. Rev. Lett.* **122**, 204301 (2019).
- [12] H. Xue, Y. Yang, G. Liu, F. Gao, Y. Chong, and B. Zhang, Realization of an Acoustic Third-Order Topological Insulator, *Phys. Rev. Lett.* **122**, 244301 (2019).
- [13] Y. Peng and G. Refael, Floquet Second-Order Topological Insulators from Nonsymmorphic Space-Time Symmetries, *Phys. Rev. Lett.* **123**, 016806 (2019).
- [14] F. Zangeneh-Nejad and R. Fleury, Nonlinear Second-Order Topological Insulators, *Phys. Rev. Lett.* **123**, 053902 (2019).
- [15] M. J. Park, Y. Kim, G. Y. Cho, and S. B. Lee, Higher-Order Topological Insulator in Twisted Bilayer Graphene, *Phys. Rev. Lett.* **123**, 216803 (2019).
- [16] O. Pozo, C. Repellin, and A. G. Grushin, Quantization in Chiral Higher Order Topological Insulators: Circular Dichroism and Local Chern Marker, *Phys. Rev. Lett.* **123**, 247401 (2019).
- [17] X.-L. Sheng, C. Chen, H. Liu, Z. Chen, Z.-M. Yu, Y. X. Zhao, and S. A. Yang, Two-Dimensional Second-Order Topological Insulator in Graphdiyne, *Phys. Rev. Lett.* **122**, 244301 (2019).
- [18] R. Chen, C.-Z. Chen, J.-H. Gao, B. Zhou, and D.-H. Xu, Higher-Order Topological Insulators in Quasicrystals, *Phys. Rev. Lett.* **124**, 036803 (2020).
- [19] C.-B. Hua, R. Chen, B. Zhou, and D.-H. Xu, Higher-order topological insulator in a dodecagonal quasicrystal, *Phys. Rev. B* **102**, 241102(R) (2020).
- [20] Y. Qi, C. Qiu, M. Xiao, H. He, M. Ke, and Z. Liu, Acoustic Realization of Quadrupole Topological Insulators, *Phys. Rev. Lett.* **124**, 206601 (2020).
- [21] B. Huang and W. V. Liu, Floquet Higher-Order Topological Insulators with Anomalous Dynamical Polarization, *Phys. Rev. Lett.* **124**, 216601 (2020).
- [22] C. Chen, Z. Song, J.-Z. Zhao, Z. Chen, Z.-M. Yu, X.-L. Sheng, and S. A. Yang, Universal Approach to Magnetic Second-Order Topological Insulator, *Phys. Rev. Lett.* **125**, 056402 (2020).
- [23] M. S. Kirsch, Y. Zhang, M. Kremer, L. J. Maczewsky, S. K. Ivanov, Y. V. Kartashov, L. Torner, D. Bauer, A. Szameit, and M. Heinrich, Nonlinear second-order photonic topological insulators, *Nat. Physics* **17**, 995 (2021).
- [24] F. Schindler, A. M. Cook, M. G. Vergniory, Z. Wang, S. S. P. Parkin, B. A. Bernevig, and T. Neupert, Higher-order topological insulators, *Sci. Adv.* **4**, eaat0346 (2018).
- [25] B.-Y. Xie, H.-F. Wang, H.-X. Wang, X.-Y. Zhu, J.-H. Jiang, M.-H. Lu, and Y.-F. Chen, Second-order photonic topological insulator with corner states, *Phys. Rev. B* **98**, 205147 (2018).
- [26] X.-D. Chen, W.-M. Deng, F.-L. Shi, F.-L. Zhao, M. Chen, and J.-W. Dong, Direct Observation of Corner States in Second-Order Topological Photonic Crystal Slabs, *Phys. Rev. Lett.* **122**, 233902 (2019).
- [27] A. E. Hassan, F. K. Kunst, A. Moritz, G. Andler, E. J. Bergholtz, and M. Bourennane, Corner states of light in photonic waveguides, *Nat. Photonics* **13**, 697 (2019).
- [28] Y. Ren, Z. Qiao, and Q. Niu, Engineering Corner States from Two-Dimensional Topological Insulators, *Phys. Rev. Lett.* **124**, 166804 (2020).
- [29] C.-A. Li, B. Fu, Z.-A. Hu, J. Li, and S.-Q. Shen, Topological Phase Transitions in Disordered Electric Quadrupole Insulators, *Phys. Rev. Lett.* **125**, 166801 (2020).
- [30] A. Agarwala, V. Juričić, and B. Roy, *Phys. Rev. Research* **2**, 012067(R) (2020).
- [31] Y. Wu, H. Jiang, J. Liu, H. Liu, and X.C. Xie, Non-Abelian Braiding of Dirac Fermionic Modes Using Topological Corner States in Higher-Order Topological Insulator, *Phys. Rev. Lett.* **125**, 036801 (2020).
- [32] J.-H. Wang, Y.-B. Yang, N. Dai, and Y. Xu, Structural-Disorder-Induced Second-Order Topological Insulators in Three Dimensions, *Phys. Rev. Lett.* **126**, 206404 (2021).
- [33] B. Liu, L. Xian, H. Mu, G. Zhao, Z. Liu, A. Rubio, and Z. F. Wang, Higher-Order Band Topology in Twisted Moiré Superlattice, *Phys. Rev. Lett.* **126**, 066401 (2021).
- [34] L. Fu, Topological Crystalline Insulators, *Phys. Rev. Lett.* **106**, 106802 (2007).
- [35] K. Shiozaki and M. Sato, Topology of crystalline insulators and superconductors, *Phys. Rev. B* **90**, 165114 (2014).
- [36] G. van Miert and C. Ortix, Higher-order topological insulators protected by inversion and rotoinversion symmetries, *Phys. Rev. B* **98**, 081110(R) (2018).
- [37] E. Cornfeld and A. Chapman, Classification of crystalline topological insulators and superconductors with point group symmetries, *Phys. Rev. B* **99**, 075105 (2019).
- [38] E. Cornfeld and S. Carmeli, Tenfold topology of crystals: Unified classification of crystalline topological insulators and superconductors, *Phys. Rev. Research* **3**,

- 013052 (2021).
- [39] E. Khalaf, H. C. Po, A. Vishwanath, and H. Watanabe, Symmetry Indicators and Anomalous Surface States of Topological Crystalline Insulators, *Phys. Rev. X* **8**, 031070 (2018).
- [40] W. A. Benalcazar, T. Li, and T. L. Hughes, Quantization of fractional corner charge in C_n -symmetric higher-order topological crystalline insulators, *Phys. Rev. B* **99**, 245151 (2019).
- [41] M. Parto, S. Wittek, H. Hodaei, G. Harari, M. A. Bandres, J. Ren, M. C. Rechtsman, M. Segev, D. N. Christodoulides, and M. Khajavikhan, Edge-Mode Lasing in 1D Topological Active Arrays, *Phys. Rev. Lett.* **120**, 113901 (2018).
- [42] X.-W. Luo and C. Zhang, Higher-Order Topological Corner States Induced by Gain and Loss, *Phys. Rev. Lett.* **123**, 073601 (2019).
- [43] Y.-J. Wu, C.-C. Liu, and J. Hou, Wannier-type photonic higher-order topological corner states induced solely by gain and loss, *Phys. Rev. A* **101**, 043833 (2020).